Full-scale two-phase flow measurements on Athena research vessel

James P. Johansen, Alejandro M. Castro, Pablo M. Carrica *

IIHR – Hydroscience and Engineering, C. Maxwell Stanley Hydraulics Laboratory, The University of Iowa, Iowa City, IA 52242-1585, United States

ABSTRACT

Measurements of gas volume fraction, bubble velocity, chord length and bubble size distributions were performed on the research vessel *Athena II* operating in Saint Andrew Bay in the gulf coast near Panama City, FL. Double tipped sapphire optical local phase-detection probes were used to acquire indicator functions downstream of the breaking bow wave, behind the masker and at the stern. These indicator functions were also taken at different depths, operating speeds and headings respect to the waves. The data processing includes the computation of velocity of individual bubbles and chord lengths, resulting in chord length distributions. These chord length distributions are used to obtain bubble size distributions using a novel procedure described in detail herein. Uncertainty analysis is performed for gas volume fraction, average bubble velocity and chord length. The results indicate that air entrainment increases with ship speed and sailing against the waves at all positions. The bow wave exhibits unsteady breaking that creates bubble clouds, which were characterized and identified by signal processing. At the stern a very strong dependence of bubble size with depth was found, with evidence that small bubbles (smaller than 500 μm) are transported through the bottom of the hull and reach the transom. The roller present at the transom, the associated strong unsteadiness and bubble entrainment are well captured, as indicated by the stern results, showing the frothy nature of the upper layer.

1. Introduction

Two-phase flows around ships have been studied for years, mostly in relation with ship acoustic signatures: ships have been tracked acoustically since before World War II (Borowski et al., 2008). Bubbles generated by the ship's bow and shoulder breaking waves, the hull/free surface contact line, the propeller and the highly turbulent stern flow are transported by the flow, forming a two-phase mixture below the hull and in the bubbly wake, which can be kilometers long. More recently, bubble-induced drag reduction has attracted increasing interest. Externally-injected bubbles have achieved drag reductions ranging from 4% to 22% in ships and flat plates (Latorre et al., 2003; Takahashi et al., 2003). Self-aeration during normal operation of a ship likely has an effect on drag, although it is very difficult to quantify since two-phase phenomena do not exhibit similarity at model scale, forcing experimentation in full scale. Though significant effort has been devoted to the study of ship's wakes and far-field measurements (see for instance Hyman, 1994; Caruthers et al., 2009), little is known about the sources of bubbles (entrainment through the free surface, cavitation, etc.) created by a ship. Near-field models have long relied on assumed bubble size distributions, like that of Cartmill and Su (1993), and entrainment locations to predict the two-phase field

(Carrica et al., 1998, 1999). Some progress has been recently made in predicting the location and intensities of the bubble entrainment (Moraga et al., 2008; Ma et al., 2009), but calibration of the models is based on simple model-scale canonical problems and validation based on ship computations and measurements has not been performed.

Near-field full-scale measurements of the two-phase flow around a ship are scarce, mostly due to the difficulties related with operating at bubble-generating speeds and instrumentation limitations. Wakes are generally measured in the earth system, where velocities are fairly small, while near-field measurements need to be made on board. Acoustic methods can be used in the far field to obtain air concentration and bubble size distributions, while in the near field the presence of the hull makes it difficult to use these methods. In one of the few near-field full scale measurements known to the authors, Terril and Fu (2008) used an array of twelve conductivity probes to measure the gas volume fraction on the highly aerated stern regions of the *Revelle* and the US Navy *Athena* research vessel II (*Athena II* R/V). Measurements for *Athena II* R/V were performed during the May 2004 campaign at different depths and lateral positions for speeds ranging from 1 to 6.6 m/s (2–12.8 knots). These measurements revealed the presence of a sharp decrease on the gas volume fraction with depth, separating the recirculating region above the transom corner with the boundary layer developed by the hull. Optical sizing measurements performed below the hull line at the transom, in regions of low

* Corresponding author. Tel.: +1 319 335 6381; fax: +1 319 335 5238.
E-mail address: pablo-carrica@uiowa.edu (P.M. Carrica).

gas volume fraction, resulted in a peak in the bubble size distribution (in *bubbles*/(m^3 μm)) for bubbles at around 15 μm in radius (Terril et al., 2005). Jeon et al. (2008) used a defocused digital particle image velocimetry (DPIV) system to measure bubble size distribution and gas volume fraction on the previously mentioned *Athena II* R/V in a May 2004 experimental campaign. The system was limited to maximum gas volume fractions of about 1% due to bubble saturation in the measurement domain, so two deep regions downstream of the transom were measured. Average bubble sizes are reported for two salinity concentrations and several speeds, ranging from 1 to 6.2 m/s (2–12 knots).

This work presents full scale measurements of gas volume fraction, bubble velocity and bubble size distribution for the *Athena II* R/V. The measurements were performed using double tipped optical local phase-detection sapphire probes, which by sensing phase interfaces provide the phase indicator function in a point in space for a period of time. Using double tipped probes allows measurement of the bubble velocity and the size distribution, after some assumptions. The two-phase parameters were measured downstream of the bow breaking wave, the aerator masker and in the highly ventilated transom stern flow, for velocities ranging from 3.1 to 6.2 m/s (6–12 knots).

The use of optical phase-detection probes provides very detailed information at a single point, but significant challenges needed to be overcome before they could be used in a full-scale ship in the ocean, including fouling, debris, and mechanical vibrations due to high drag forces. Glass fiber optics probes are relatively easy to manufacture with small active tips (see for example Hoschek et al., 2008), but are fragile and therefore unsuitable for full-scale ship experiments. Sapphire probes are significantly more difficult to build, but offer a remarkable resilience compared to glass probes. Former applications in hostile environments include study of aeration ditches (Vermande et al., 2007), steam/water flows (Yoneda et al., 2002) and unsteady cavitation (Stutz and Reboud, 1997). Most studies found in the literature use sapphire probes manufactured by RBI in Meylan, France. In this work two types of sapphire probes from RBI are used, made from polished 375 μm and 390 μm sapphire rods. In addition, the authors manufactured a smaller probe made of 125 μm sapphire fiber which provided less intrusiveness resulting in a better cross-correlation.

This paper is organized as follows: In Section 2 the ship and onboard instrumentation, the positioning system, the different probes and associated electronics are described. Section 3 discusses the methodology used to filter the indicator functions and the methods used to obtain gas volume fraction, bubble velocity and bubble size are included, as well as uncertainty analysis. The data reduction process presented herein is novel and is explained in detail. In Section 4 the different tests performed are presented. The results discussed are organized according to the regions of measurement: bow wave, masker and stern. The limitations, possible improvements for future at-sea campaigns and overall conclusions are discussed in Section 5.

2. Experimental

The experiments were performed on the US Navy research vessel *Athena II*, a decommissioned PG-84 Asheville-class patrol gunboat transformed into a high-speed research vessel in 1976 (Fig. 1). The water line length of Athena is $L = 47$ m, with a beam $B = 7.32$ m and a design draft $T = 3.2$ m. The *Athena II* has an aluminum hull, resulting in a water displacement of 240 tons. Propulsion is provided by twin counter-rotating propellers of variable pitch, powered either by two independent diesel engines or a GE LM 1500 gas turbine, allowing the vessel to reach maximum speeds of 6.7 or 18 m/s using diesel or gas turbine, respectively. The *Athena II* R/V is fitted with a skeg, starboard and port roll stabilizers, and a compound masker system to entrain bubbles and reduce the ship's radiated noise (none of these are shown in the schematic in Fig. 1). The masker is a ring fitted around the hull at approximately $x/L = 0.45$. Bubbly white water produced by the masker can be seen in Fig. 1.

The measurement campaign took place in Panama City, FL, where the *Athena II* R/V is based, in the week of April 20–24, 2009. Measurements were taken Tuesday through Friday in Saint Andrews Bay and in the Gulf of Mexico several miles offshore but within sight from the coast. Measurements were taken at the positions shown in Fig. 2, located downstream of the unsteady breaking bow wave, the starboard masker and the port side of the stern.
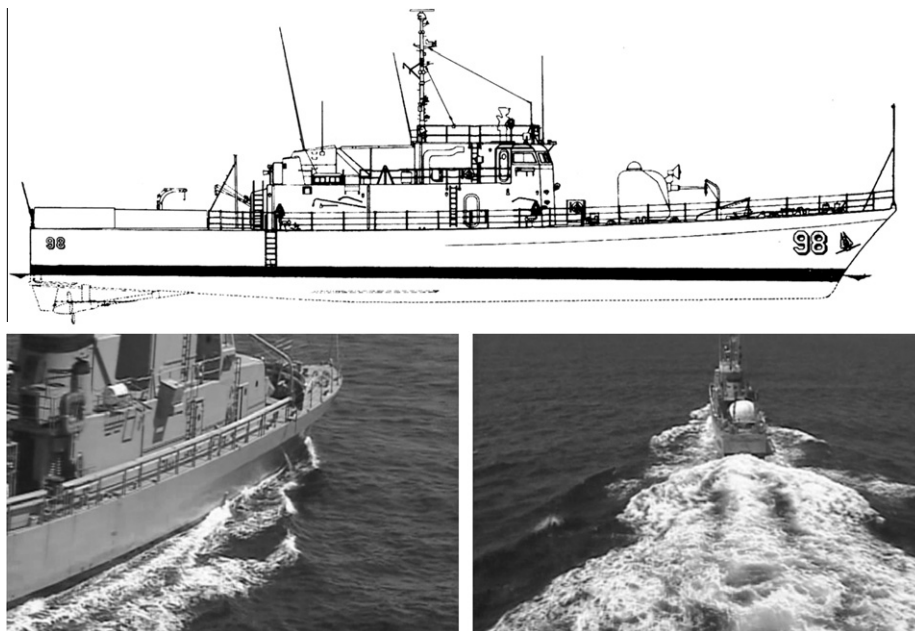

Fig. 1. Athena R/V. Top: schematic of the ship, waterline and appendages. Bottom left: view of the bow wave and the masker. Bottom right: bubbly wake produced by the ship.
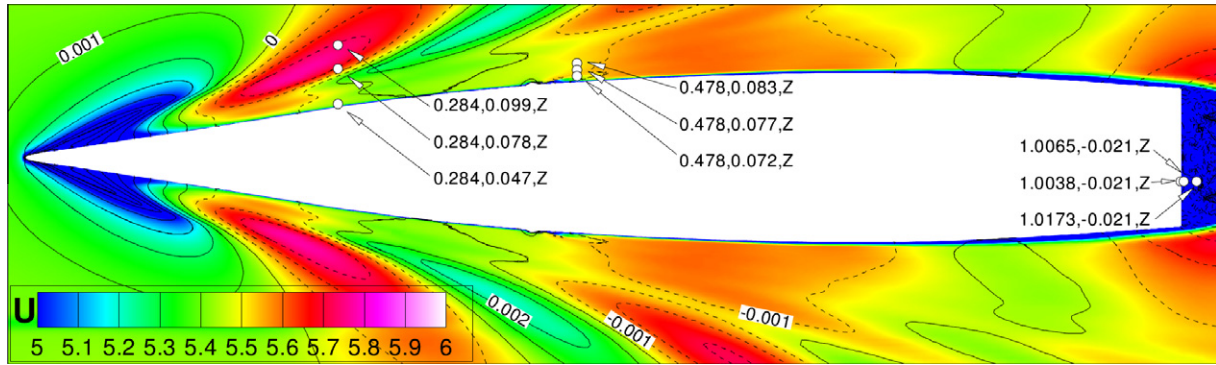
Fig. 2. Athena R/V profile at waterline showing probe measurement locations and free surface.

2.1. Optical phase-detection probes

Optical phase-detection probes are used to measure the phase indicator function, defined as (Ishii, 1975)

$$\chi(\mathbf{r}, t) = \begin{cases} 1 & \text{if the probe tip is in air} \\ 0 & \text{if the probe tip is in water} \end{cases} \tag{1}$$

while some information on the instrumentation used is provided herein, the working principles of optical phase-detection probes are discussed in detail elsewhere (Cartellier and Achard, 1991; Barrau et al., 1999).

The instrumentation for one channel (one probe tip) is composed by optical and electronic modules, consisting of a light source, a photodetector and an optical fiber connector for the probe itself, with a fiber optic coupler connecting all these components, plus amplifiers, signal conditioners and comparators. The light source directs light into a fiber optic connected to a coupler, which works as a beam splitter. This beam splitter sends 50% of

the incoming light to an optical fiber connector to which the probe is attached. Due to refraction index variations between air and water and the conical shape of the probe tip, more light is reflected back to the coupler when the probe tip is in air. The coupler transmits a fraction of the light that is reflected from the probe back to the photodetector which converts light into electric signals that are then conditioned and amplified. The analog signals are subsequently transformed into binary phase indicator functions using a double threshold technique (Cartellier and Achard, 1991). In this work RBI infrared optoelectronic modules were used.

Three probes were employed in the experiments. For the masker and transom measurements a double sapphire tip RBI probe was used, made of 375 μm sapphire rod polished to a cone of about 15° down to a tip finished with a 45° cone with an effective radius of about 30 μm, see Fig. 3a and c. For the measurements in the bow, a smaller double probe was constructed using 125 μm sapphire fiber polished to a 45° cone on the tip (Fig. 3a and c), resulting in a less intrusive system with better cross-correlation between the two tips of the probe. The short sapphire fiber was polished to
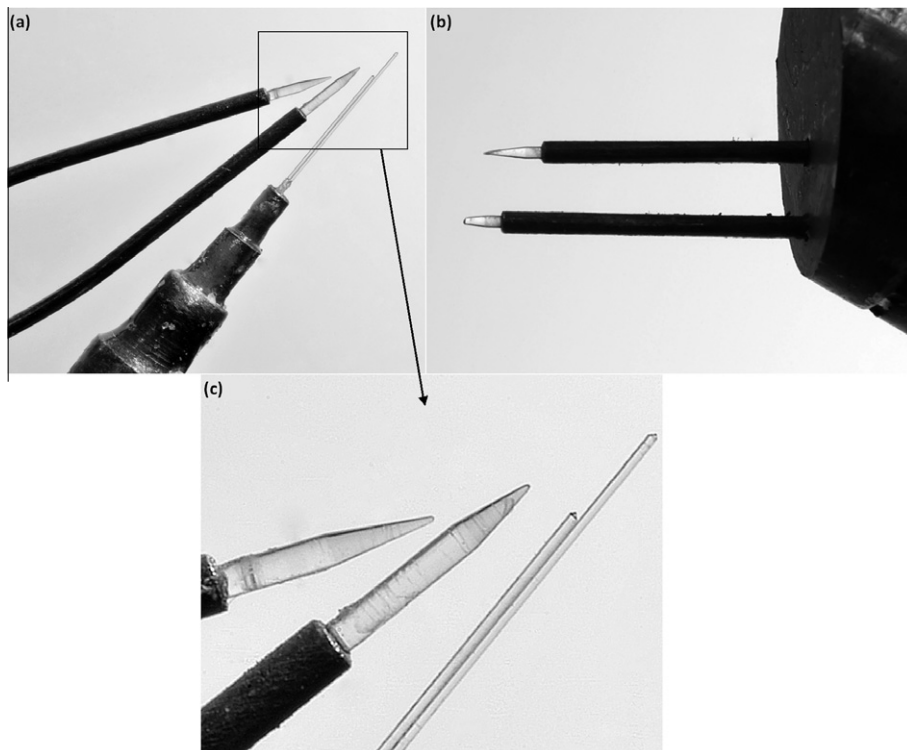

Fig. 3. Optical probes. (a) RBI (left) and IIHR (right), (b) RBI II, (c) close-up of the tips of RBI and IIHR probes.

90° on the end opposite the polished cone and spliced with a glass fiber with 100/140 μm core/cladding diameters made by TLC/Corning. A second, sturdier probe made by RBI with 390 μm sapphire rod was also used for measurements at the bow under rougher seas, see Fig. 3b. This probe is hereafter referred to as RBI II. The distance between tips for the RBI probe was 1.2 mm, 2.25 mm for the RBI II probe, and 1.32 mm for the IIHR probe.

In the RBI system the binary signals from each of the channels are fed to a USB card (1 μs resolution) that connects directly to a laptop PC. RBI proprietary software ISO was used to acquire the data, which were stored for off-line analysis. The overall instrumentation was mounted in sturdy aluminum cases consisting of four optoelectronic channels, oscilloscopes for monitoring the analog signals, a UPS backup power module, a USB card and a multimeter to monitor the threshold levels.

From the indicator function, the time-averaged gas volume fraction is computed from:

$$\alpha(\mathbf{r}) = \frac{1}{T} \int_0^T \chi(\mathbf{r}, \tau) d\tau \qquad (2)$$

where T is the averaging period. T has to be long enough such that the gas volume fraction converges to a steady value. Following Carrica et al. (1995), this means that enough bubbles are measured and that the integration time is significantly longer than the characteristic time of whatever transient physical process is occurring in the two-phase flow. To converge other variables, such as the bubble size distribution, significantly longer times are needed. In this work measurement times ranges from 1 to 3 min, limited by the ability of the ship to maintain steady conditions. In most conditions several measurements were taken to check repeatability and to reduce statistical errors, as discussed later.

2.2. Positioning system

The probes were deployed using a pole made of thick-walled steel tube 25.4 mm in diameter, with the last meter of the measuring end reduced to a 12.7 mm diameter. The probes were attached to the end of the pole on the ship's deck. Steel brackets were held to the 50.8 mm stanchions (handrail poles), allowing measurement at several locations along the hull. The brackets were fitted with two extensible hinged arms that permitted positioning of the probe normal to the hull. The pole with the probe could slide vertically along tubes attached to the extensible arms to allow for vertical positioning. Once the probe was set in place the arms and pole were immobilized using set screws. To perform measurements at the stern, where no stanchions are available, a 50.8 mm vertical tube was attached to existing brackets welded on the transom face of the hull, and then the same positioning system was used.

3. Data processing

The measurements provided two indicator functions, corresponding to each tip of the probe used. These indicator functions were processed to account for stratification, to obtain gas volume fraction, bubble velocity, bubble size distribution, and to identify bubble clouds.

3.1. Raw indicator function

Fig. 4a shows eight seconds of the indicator functions measured at the bow with the IIHR probe. An excellent correlation between the probes can be observed, helped by the small size of the probe tips and by the high bubble velocity. As shown in Eq. (1), a logical level of 1 corresponds to the air phase. Fig. 4b shows a larger view of a typical single bubble event with the times of phase change displayed. Defining the rising and falling times for the same bubble i for Probe Tip 1 as $(t1_{i+}, t1_{i-})$ and for Probe Tip 2 as $(t2_{i+}, t2_{i-})$, the time the probe tip was inside each bubble can be found on an event by event basis for Probe Tip 2 $\Delta t1_i$ and Probe Tip 2 $\Delta t2_i$ as

$$\Delta t1_i = t1_{i-} - t1_{i+} \qquad (3)$$
$$\Delta t2_i = t2_{i-} - t2_{i+} \qquad (4)$$

Notice in Fig. 4a that there is large time period in air starting at the 18.3 s mark indicating that the probe was out of the water for a period of time. This happened when the probe was very close to the air/water interface, due to the presence of small waves, or when the free surface was highly unsteady, as in the stern region.

3.2. Indicator function filtering

The first step in signal processing is the removal of the time when the probe breaks the free surface. The probe is no longer in the air water mixture resulting in artificially higher recorded gas volume fraction. The logical filter expression is

$$\text{If: } \Delta t1_i > \frac{CL_{max}}{V_{ship}}$$
$$\text{then: } \Delta t1_i = out\ of\ water\ time$$

where CL_{max} is the maximum bubble chord length, set to 10 mm, and V_{ship} is the ship velocity. The new filtered gas volume fraction $\alpha1_{filter}$ expression is
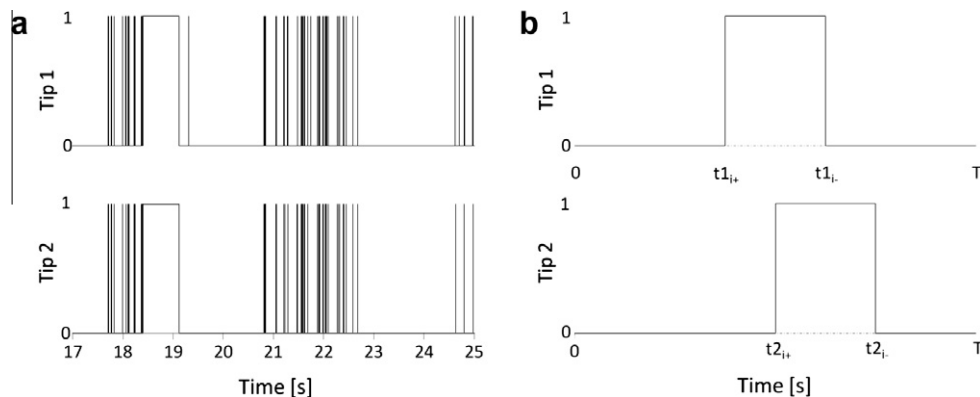

Fig. 4. (a) Typical indicator functions from experimental data sample, (b) larger view of an idealized single bubble event in both probe tips.

$$\alpha 1_{filter} = \frac{\sum_{i=1}^{N_1 - N_{1o}} (\Delta t1_i)[in\ water] - \sum_{i=1}^{N_{1o}} (\Delta t1_i)[out\ of\ water]}{T - \sum_{i=1}^{N_{1o}} (\Delta t1_i)[out\ of\ water]} \quad (5)$$

where T is the sampling time, N_1 is the number of bubbles detected by Tip 1 and N_{1o} is the number of out-of-water events.

The measured indicator functions for both tips do not correlate exactly, i.e. the signal of the second probe is not a perfect shift in time of the signal of the first probe. Herein we attempt to pair the bubbles detected by Tip 1 to those of Tip 2 by applying a series of filters to the indicator functions. This allows determination of velocity and chord length for each bubble, and the corresponding bubble velocity and size distributions. Four logical filters are used for this purpose.

The first logical filter is to limit possible accepted bubble velocities by assuming that the probe is in the direction of the flow and there is a range of velocity fluctuations around the velocity obtained by cross-correlation of the signal, V_{cc}. A range V_Δ of approximately ±3 m/s around the cross-correlation velocity was used on the bow and masker sections of the ship. In the stern section the range of bubble velocities increased due to the more complex multidirectional flow structures. The logical expression is

> *if*: $V_{cc} - V_\Delta < V_i < V_{cc} + V_\Delta$
>   *then*: *Accept Bubble Possibility*
>   *else*: *Reject Bubble Possibility*

where the bubble velocity can be found by using the rising or the falling times and by knowing the distance between probe tips (L)

$$V_{r,i} = \frac{L}{(t2_{i,+} - t1_{i,+})} \quad (6)$$

$$V_{f,i} = \frac{L}{(t2_{i,-} - t1_{i,-})} \quad (7)$$

Assuming a flat gas/water interface in the bubble and the probe tips and interface are directly aligned with the flow, the bubble rising time velocity V_r and the bubble falling time V_f should be equivalent. In reality the probe tips are not perfectly aligned to the flow and the interface is curved, resulting in that the bubble time recorded by Probe Tip 2 was different from the bubble time recorded by Probe Tip 1. In this work we use the average of the rise time and fall time velocities as the individual bubble velocity

$$V_i = \frac{V_{r,i} + V_{f,i}}{2} \quad (8)$$

In the velocity range between the minimum and maximum accepted velocities there are accepted bubble possibilities that are undesirable. One instance of an undesirable bubble occurs when the probe breaks the free surface. The probe views this occurrence as one large bubble. This would result in unrealistic chord length distances that skew the average chord length of all the bubbles to a larger value. These surface breaks are filtered out easily enough by checking the chord length CL_i or chord time Δt_i. The chord length for bubble i is computed from the average of the chord length obtained for Probe Tips 1 and 2 as

$$CL_i = V_i \, \Delta t_i \quad (9)$$

with the bubble chord time defined as the average of the values measured by the tips

$$\Delta t_i = \frac{\Delta t1_i + \Delta t2_i}{2} \quad (10)$$

A filter is then applied as

> *if*: $CL_{max} < CL_i$
>   *then*: *Reject Bubble Possibility*
>   *else*: *Accept Bubble Possibility*

After filtering unacceptable bubble velocities and sizes there are still other possibilities that need to be evaluated. Fig. 5a shows a situation in which two bubble events hit both probe tips very closely together in time resulting in an anomaly that can pass the previous two logical checks creating four possible bubble combinations. These situations are easy to identify because the events have to be used twice to make up the four bubble possibilities.

$$\begin{aligned}
(a)\ &\Delta t1_1 \sim \Delta t2_1 \\
(b)\ &\Delta t1_1 \sim \Delta t2_2 \\
(c)\ &\Delta t1_2 \sim \Delta t2_1 \\
(d)\ &\Delta t1_2 \sim \Delta t2_2
\end{aligned} \quad (11)$$

Only two of the combinations can be chosen to eliminate the re-use of bubble events, (a) and (d) or (b) and (c). (a) and (d) is the correct choice, because for (b) and (c) to occur, the two bubbles in question would have to switch positions in the time it takes to travel between the probe tips. The assumption is made that this occurrence is unlikely so combinations are filtered to a chronological condition.

There is still one situation shown in Fig. 5b that can elude the previous three logical filters. It is the situation where there are two combinations possible due to an extra event in one probe tip that does not get recorded in the second probe tip or vice versa. This is caused by a non perfect signal correlation. The combinations are

$$\begin{aligned}
(a)\ &\Delta t1_1 \sim \Delta t2_1 \\
(b)\ &\Delta t1_2 \sim \Delta t2_1
\end{aligned} \quad (12)$$

In this situation the combination is selected that would have the closest velocity to the average of the previously accepted bubbles V_{ave}. Comparing chord times is an option but velocity measurements are much more steady than the chord time measurements so V_{ave} was chosen as the velocity for the logical expression shown below:

> *if*: $|V_{comb,a} - V_{ave}| < |V_{comb,b} - V_{ave}|$
>   *then*: *Accept Combination a*
>   *else*: *Accept Combination b*

This results in an iterative process since V_{ave} changes slightly after the logical loop above. With a good indicator function correlation the need for this logical loop becomes rare and most bubbles are accepted by the first three logical filters. Notice also that to avoid double-counting, once a bubble has been identified in the signals from Probe Tips 1 and 2, these bubble events are not available to pair with other events.

3.3. Gas volume fraction, velocity, and chord length

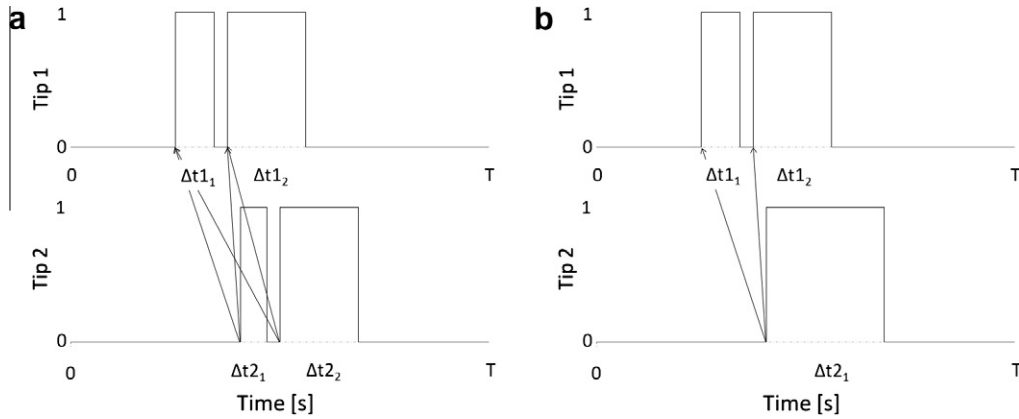The time-averaged gas volume fraction for each probe can be found as

Fig. 5. Indicator function events that need filtering. (a) Repeated use of events resulting in four combinations. (b) Repeated use of bubble events resulting in two combinations.

$$\alpha 1 = \frac{1}{T} \sum_{i=1}^{N_1} (\Delta t 1_i) \tag{13}$$

$$\alpha 2 = \frac{1}{T} \sum_{i=1}^{N_2} (\Delta t 2_i) \tag{14}$$

while the gas volume fraction filtered by out of water events is computed as in Eq. (5). Notice that the number of bubbles pierced by both probes may differ, and that the number of bubbles accepted after filtering may reject some bubbles from Probe Tip 1, 2, or both. Because Tip 1 is less intrusive than Tip 2, which is affected by Tip 1, the gas volume fraction from Tip 1 has been used throughout the paper, either filtered as in Eq. (5) or unfiltered as in Eq. (13).

The procedure described previously provides velocity and chord length for each individual bubble. The average bubble velocity and chord length are computed as

$$\overline{V} = \frac{1}{N} \sum_{i=1}^{N} V_i \tag{15}$$

$$\overline{CL} = \frac{1}{N} \sum_{i=1}^{N} CL_i \tag{16}$$

where N is the number of accepted bubbles.

3.4. Bubble clouds identification and attribute calculation

Visual observation at the bow clearly indicated the presence of bubble clouds formed during unsteady breaking of bow waves. The clouds can be easily recognized in the indicator functions. The average length of the clouds, along with the in-cloud bubble velocity, chord length, and gas volume fraction, are desired attributes to characterize the two-phase flow in the bow. While visual identification is easy, a standard definition of a cloud needs to be set to isolate the clouds from the indicator functions gathered from the experiments. The indicator function inside the clouds is used to compute a gas volume fraction for the cloud. A cloud is defined as a grouping of 10 or more bubbles that have rising edges separated by less than 0.75 m. This means that in a bubble cloud there cannot be a gap between two consecutive bubbles of more than 0.75 m, with this distance computed using the ship velocity V_{ship}. The resulting process creates a cloud indicator function, that can be used as a conditional to the indicator function to compute in-cloud properties, as shown in Fig. 6.

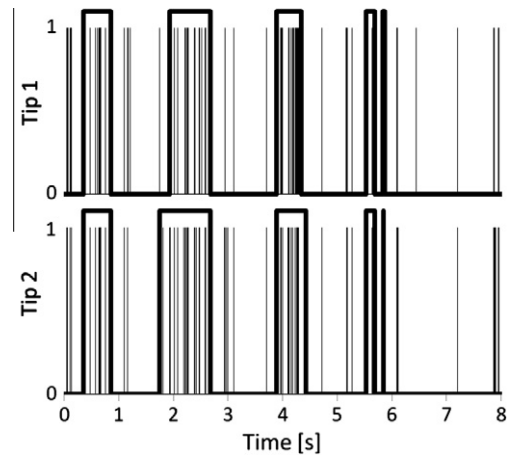The bubble cloud indicator function was created by the following logic

Fig. 6. Indicator functions for two probe tips with the bubble clouds outlined in bold by a secondary cluster indicator function. This specific data set was acquired at the bow, 0.2 m below the free surface with the Athena R/V traveling at 5.4 m/s (10.5 knots) using the IIHR probe.

> *Assume*: The tip is in air
> *if*: $(t1_{i+2} - t1_i) > \frac{0.75 \text{ m}}{V_{ship}}$
>   *then*: $t1_i$–$t1_{i+2}$ is in water
>   *repeat*: Step i by 2
> *if*: $Section_{air,i}$ contains < 10 bubbles
>   *then*: $Section_{air,i}$ is not a cloud **&** $Section_{air,i}$ is in water

This expression begins with the cloud indicator function in air, and then finds the spaces between rising edges of bubbles that have a greater distance than 0.75 m between them and sets that section to water. The next logical expression identifies the sections in air ($|(Section)|downarrow(air, i)$) that do not contain at least 10 bubbles and sets that section to a value that denotes water. The remaining sections in air make up the cloud outline that creates the cloud indicator function.

The time duration of the cloud is obtained in the same way the time is calculated when a probe tip passes through an individual bubble, see Eq. (3), but by using the cloud indicator function:

$$\Delta Ct 1_j = Ct 1_{j-} - Ct 1_{j+} \tag{17}$$

The in-cloud gas volume fraction allows for a comparison of the gas volume fraction of the cloud compared to overall time-averaged gas volume fraction in Eq. (13). For cloud j the in-cloud gas volume fraction is

$$\alpha 1_j = \frac{1}{\Delta Ct1_j}\sum_{i=1}^{N_j}(\Delta t1_i) \tag{18}$$

The length of a cloud is defined by

$$L_j = V_{ship}\,\Delta Ct1_j \tag{19}$$

The averages of the bubble velocities and the bubble chord lengths within the clouds serve as a way to compare the bubbles in the clouds to the data sample as a whole. The average in-cloud bubble velocity and chord length are defined as

$$\overline{V}_j = \frac{1}{N_j}\sum_{i=1}^{N_j} V_i \tag{20}$$

$$\overline{CL}_j = \frac{1}{N_j}\sum_{i=1}^{N_j} CL_i \tag{21}$$

where N_j is the number of bubbles in-cloud j.

3.5. Bubble size distribution

A distribution of chord lengths obtained by a probe can be transformed into a distribution of bubble radii by assuming that the bubbles are spherical. The number of counts found in a certain chord length interval $(c, c + dc)$ are the combined result of the probability of hitting a bubble of diameter D and the probability that the piercing of this bubble will happen with a chord length c. The number of counts found in this interval will be the combination of several events. For instance, some events may include hitting bubbles with diameter c right through their center line, while other events may include piercing larger bubbles through the side such that the length traveled by the probe is still c. This situation is outlined in Fig. 7. The problem of finding the bubble size distribution of spheres $P(D)$ from the chord length distribution is known as *unfolding*. Classical approaches to this problem are presented in Takeo (1971), Clark and Turton (1988), Liu and Clark (1995), Liu et al. (1998) and Hu et al. (2006). The most important effect differencing the chord length from the size distribution is that the probe *detects* larger bubbles with more frequency than are present in the fluid just because their cross sectional area is larger. Another cause affecting the distributions is the finite probe size, which is unable to detect bubbles with diameter smaller than
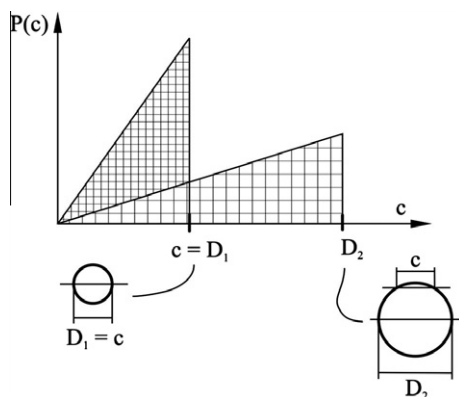
approximately the probe diameter. In this regard, a model for the probe size is developed and experimental proof is presented showing that this effect cannot be neglected.

3.5.1. Chord length distribution

The objective of the unfolding process is to find the bubble size distribution $f(D, \mathbf{x}, t)$, in $bubbles/(m^3\ \mu m)$. An optical probe provides information along a 1D trajectory through which bubbles travel. The correction necessary to account for this is called herein the *3D correction*. The bubble size distribution can be expressed as

$$f(D, \mathbf{x}, t) = N(\mathbf{x}, t)P(D, \mathbf{x}, t) \tag{22}$$

where N is the number density in $bubbles/m^3$ and $P(D)$ has units of μm^{-1}. The number density and gas volume fraction can be found in terms of the number density distribution as

$$N(\mathbf{x}, t) = \int_0^\infty dD f(D, \mathbf{x}, t)$$
$$\alpha(\mathbf{x}, t) = \int_0^\infty dD \frac{\pi}{6}D^3 f(D, \mathbf{x}, t) \tag{23}$$

The probability of having a chord length c after impact of a spherical bubble of diameter is (Clark and Turton, 1988)

$$P(c|D) = \frac{2c}{D^2}H(c - D) \tag{24}$$

where $H(x)$ is the Heaviside function. Thus, a monodisperse size distribution measured by an optical probe results in a triangular chord length distribution. If the probe has a diameter p, we assume that bubbles with D smaller than p cannot be pierced by the probe. The selection of p is reasonable but somewhat arbitrary, since unquestionably high speed bubbles can be pierced by bigger probes and slower ones will resist piercing. With this model the minimum chord length that can be obtained when piercing a bubble with diameter D occurs when the probe center is located at a distance $p/2$ from the bubble edge as shown in Fig. 8. From a geometrical analysis this minimum chord length is

$$c_p(D) = \sqrt{p(2D - p)} \tag{25}$$

Then,

$$P_p(c|D) = \frac{P(c|D)H(c - c_p)H(D - c)}{\int_{c_p}^{D} dcP(c|D)} \tag{26}$$

and using Eq. (24) yields

$$P_p(c|D) = \frac{2c}{(D - p)^2}H(c - c_p(D))H(D - c) \tag{27}$$

Consider now a possible trajectory of the probe in which it travels a distance L, see Fig. 9. A bubble of diameter D will be hit by the probe if its center is at a distance $d = R - p/2$ from this trajectory. Then, the probe will only hit bubbles that are inside a tube of length L and an effective cross sectional area $A_{eff} = \frac{\pi}{4}(D - p)^2$. The number of bubbles with diameter in the interval $(D, D + dD)$ inside this tube is
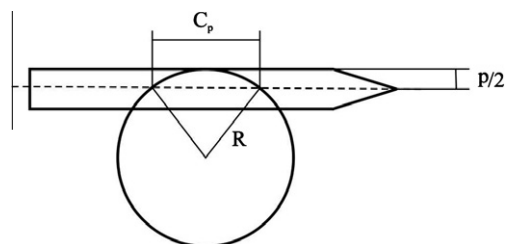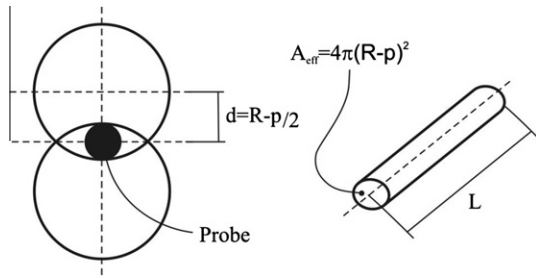

Fig. 7. Counts in the chord length distribution at a certain chord length c product of hitting bubbles with a diameter $D_1 = c$ and larger bubbles with diameter D_2.

Fig. 8. Situation of minimum chord size C_p, happening when the probe edge is tangent to the bubble's interface.

Fig. 9. The probe will hit bubbles if its circumference is completely included inside the bubble cross section.

$$n(D)\,dD = N\,LA_{eff}P(D)dD \tag{28}$$

A fraction $P_p(c|D)$ of these bubbles produces counts in the chord length c so that $n(D)\,dDP_p(c|D)\,dc$ is the contribution to chord lengths in $(c, c + dc)$ from bubbles of diameters $(D, D + dD)$. Integration over all bubble sizes results in the total number of counts in $(c, c + dc)$

$$n(c) = dc \int_0^\infty dDP_p(c|D)\,n(D) = \int_c^{c_p^{-1}(c)} dDP_p(c|D)\,n(D)$$

$$= NL\frac{\pi c}{2} \int_c^{c_p^{-1}(c)} dDP(D) \tag{29}$$

where $c_p^{-1}(c) = \frac{c^2+p^2}{2p}$.

The total number of bubbles pierced by the probe can be computed by integration of Eq. (28)

$$N_h = \int_p^\infty dD\,n(D) = NL \int_p^\infty dDA_{eff}(D)P(D) = NL\overline{A}_{eff} \tag{30}$$

where $\overline{A}_{eff} = \int_p^\infty dDA_{eff}(D)P(D)$. The chord length distribution will be the quotient of the number of pierced bubbles in $(c, c + dc)$, Eq. (29), with the total number of pierced bubbles, Eq. (30). Omitting the differential dc

$$P(c) = \beta c \int_c^{c_p^{-1}(c)} dDP(D)$$

$$\beta = \frac{\pi}{2\overline{A}_{eff}} \tag{31}$$

The validity of Eq. (31) was verified by conducting simulations of synthetic probe signals obtained from a known size distribution of bubbles inside a box. This expression naturally includes the 3D correction and also provides an explicit form for the computation of the constant β. In Hu et al. (2006) the 3D correction is also considered and they arrive to the same form of Eq. (31) but the a finite sized probe is not considered. Ignoring the 3D correction would lead to gross errors if the size distributions deviate significantly from mono disperse, as it is the case herein.

3.5.2. Properties of the transformation

Before inverting Eq. (31) some properties of the transformation are analyzed. In the limit $p \to 0$ Eq. (31) reduces to

$$P(c) = \beta c \int_c^\infty dDP(D) \tag{32}$$

and $P(c)$ can be obtained from

$$\frac{d}{dc}\left(\frac{P(c)}{c}\right)\bigg|_{c=D} = -\beta P(D) \tag{33}$$

In this case the inverse problem can easily be solved. However, the direct use of Eq. (33) to solve the problem involves taking the derivative of experimental data; any noise in the experimental data will result in extremely amplified noise in the inverse solution. Researchers have had problems in finding an inverse solution free of noise. Even starting by discretizing Eq. (32) and solving a system of equations, the numerical discretization is still an approximation of the derivative in Eq. (33). Another important observation is that since $P(D)$ is a probability density function it is positive, then from Eq. (33)

$$\frac{d}{dc}\left(\frac{P(c)}{c}\right) < 0 \tag{34}$$

Eq. (34) means that $P(c)/c$ is a monotonically decreasing function of c. Fig. 10a shows $P(c)/c$ obtained from experimental data taken at the bow of Athena II R/V. We see that $P(c)/c$ is not monotonically decreasing as it should be to produce a positive diameter distribution. Similar results are obtained with any other set of the experimental data taken. The inconsistency is resolved by introducing a finite size probe, which causes $P(c)/c$ to decrease for small c, as occurs in the experimental data. Fig. 10b shows the effect of finite size probe tip on $P(c)$ and $P(c)/c$ for an arbitrary exponentially decreasing $P(D)$. While an infinitesimally small probe shows a monotonically decreasing $P(c)/c$, a 125 μm probe tip results in a distribution much closer to those found in the experiments.

3.5.3. Unfolding of the bubble size distribution

The constant β in Eq. (31) is not known a priori. Defining $\widetilde{P(D)} = \beta P(D)$ yields

$$P(c) = c \int_c^{c_p^{-1}(c)} dD\,\widetilde{P(D)} \tag{35}$$

The size distribution can be found by solving for $\widetilde{P(D)}$ and normalizing to 1.
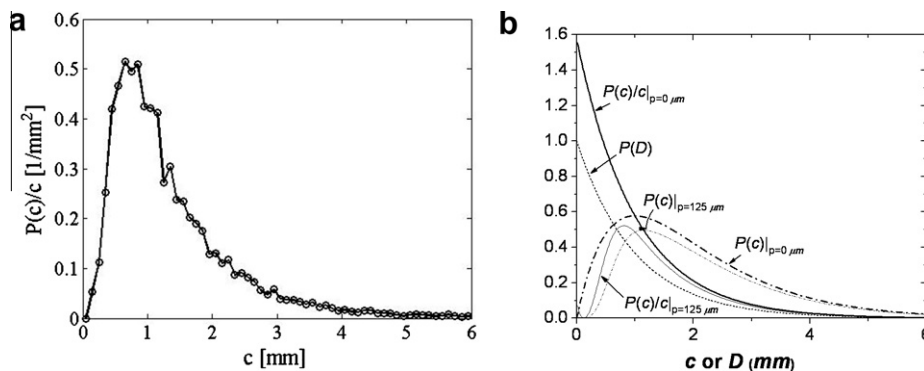
Fig. 10. (a) $P(c)/c$ for data taken at the bow of Athena R/V at $z = -0.1$ m. Note that $P(c)/c$ is not monotonically decreasing with c, (b) $\widetilde{P}(D)$ for an arbitrary size distribution function, and corresponding $P(c)$ and $P(c)/c$ for probe tips 0 and 125 μm in diameter.

When performing an experiment the results are not the continuous chord size distribution $P(c)$ but a histogram that gives the number of counts in a chord interval $\Delta c_g = c_{g+1} - c_g$. The chord size is discretized in G_c intervals with g going from 1 to $G_c + 1$. In order to compare with the experimental histograms we define

$$P_{cg} = \int_{c_g}^{c_{g+1}} dc\, P(c), \quad g = 1 \text{ to } G \tag{36}$$

The minimum and maximum chord sizes will be $c_1 = p$ and $c_{G_c+1} = c_{max}$ where c_{max} is the maximum chord size in the experimental histogram. P_{cg} and $\widetilde{P(D)}$ are then related by

$$P_{cg} = \gamma_g(\widetilde{P(D)}) = \int_{c_g}^{c_{g+1}} dc\, c \int_c^{c_p^{-1}(c)} dD\, P\widetilde{(D)} \tag{37}$$

The diameters are discretized in G_D intervals. The maximum diameter is $D_{G_D+1} = D_{max}$ and the minimum diameter is $D = p$ since bubbles smaller than p cannot be detected. The maximum diameter is chosen to be the maximum chord length. It is assumed that $P(D_{G_D+1}) = 0$. Using a piecewise linear approximation for the bubble size distribution yields

$$P(D) = \sum_{g=1}^{G_D} P_g \gamma_g(D) \quad \text{on} (p, D_{max}) \tag{38}$$

where $\gamma_g(D)$ is the hat function

$$\gamma_g(D) = \begin{cases} \frac{D - D_{g-1}}{D_g - D_{g-1}} & D_{g-1} < D < D_g \\ \frac{D_{g+1} - D}{D_{g+1} - D_g} & D_g < D < D_{g+1} \\ 0 & \text{Otherwise} \end{cases} \tag{39}$$

In this way $P(D_g) = P_g$. Substituting Eq. (38) into Eq. (37), and since $\mathscr{F}$ is a linear operator yields

$$P_{cg} = \sum_{g'=1}^{G_c} P_{g'} \mathscr{F}(\gamma_{g'}(D)) \tag{40}$$

The weights $\mathscr{F}(\gamma_g(D))$ can be computed analytically and then Eq. (40) provide G_c equations with G_D unknowns. Typically in the experiments the number of bins in the chord length histogram, G_c, was around 100 and the number of unknowns was set to around eight. Then, in order to solve this system of equations we used a least squares procedure. That is, if the measured histogram is P_{cg}^m, the following norm is minimized:

$$F = \sum_{g'=1}^{G} (P_{cg'} - P_{cg'}^m)^2 \tag{41}$$

Note that Eq. (38) provides a smooth approximation to $P(D)$. As the number of diameters G_D is increased the residual in Eq. (41) goes to zero, and will be exactly zero when $G_D = G_c$, but also the noise in $P(c)$ will be gradually amplified into noise in $P(D)$. The appropriate value for G_D that provides reasonable smooth distributions with as many points as possible is found by trial and error.

3.6. Uncertainty analysis

The ASME PTC 19.1-2005 Test Uncertainty Standards and Guidelines (ASME, 2005) were followed in the error and uncertainty analysis. A summary of the methodology is presented initially, and then uncertainty evaluations for ship speed, probe depth, bubble velocity, chord length and gas volume fraction are presented separately. Uncertainty estimation on chord length or bubble size distributions has not been attempted.

3.6.1. Uncertainty assessment methodology summary

Measurement error is the difference between a measured value and its true value. The two components of this error are the random error and the systematic error. The combined standard uncertainty is

$$\mu_{\bar{x}} = \sqrt{b_{\bar{x}}^2 + s_{\bar{x}}^2} \tag{42}$$

where $b_{\bar{x}}$ is the systematic standard uncertainty and $s_{\bar{x}}$ is the random standard uncertainty,

$$b_{\bar{x}} = \sqrt{\sum_{k=1}^{K} b_{\bar{x}_k}^2} \tag{43}$$

$$s_{\bar{x}} = \frac{T_{\nu,95}\, s_x}{\sqrt{N}} \tag{44}$$

and $\bar{x}$ represents the arithmetic mean of N samples,

$$\bar{x} = \frac{1}{N} \sum_{i=1}^{N} x_i \tag{45}$$

In Eqs. (43)–(45), $b_{\bar{x}_k}$ represents elemental systematic standard uncertainties, K represents the total number of elemental systematic standard uncertainties identified, N is the number of repeated measurements, $T_{\nu,95}$ is the student's T value with $\nu = N - 1$ the number of degrees of freedom for a 95% confidence interval, and s_x represents the standard deviation,

$$s_x = \sqrt{\sum_{i=1}^{N} \frac{(x_i - \bar{x})^2}{N-1}} \tag{46}$$

For a result R calculated by an equation containing several independent parameters $\bar{X}_j$, such that $R = f(\bar{X}_1, \bar{X}_2, \ldots, \bar{X}_J)$, the uncertainty is computed using error propagation, where

$$\mu_R = \sqrt{b_R^2 + s_R^2} \tag{47}$$

with b_R the systematic standard uncertainty and s_R the random standard uncertainty of the result, computed as

$$b_R = \sqrt{\sum_{j=1}^{J} (\theta_j b_{\bar{x}_j})^2} \tag{48}$$

$$s_R = \sqrt{\sum_{j=1}^{J} (\theta_j s_{\bar{x}_j})^2} \tag{49}$$

where $b_{\bar{X}_j}$ and $s_{\bar{X}_j}$ are the systematic and random standard uncertainties, respectively computed as in Eqs. (43) and (44), and θ_j is the sensitivity coefficient of a parameter j,

$$\theta_j = \frac{\partial R}{\partial \bar{x}_j} \tag{50}$$

3.6.2. Bubble velocity

The bubble velocity is computed from Eqs. (6)–(8), and depends on the length between probe tips L and the time it takes for a bubble to cross both probes tips. The uncertainty for the velocity of one bubble is computed from the error propagation expression

$$\mu_{v_i}^2 = \left(\frac{\partial V_i}{\partial L} B_L\right)^2 + \left(\frac{\partial V_i}{\partial t} B_r\right)^2 \tag{51}$$

where B_r is the time resolution error. Since the sampling rate of the data acquisition system was 1 MHz, the systematic standard resolution uncertainty is

$$B_r = \frac{Sample\ Rate}{2} = 0.5 \times 10^{-6}\ \text{s} \tag{52}$$

The individual bubble velocity uncertainty is then

$$\mu_{v_i}^2 = \left(\frac{1}{t}B_L\right)^2 + \left(\frac{-L}{t^2}B_r\right)^2 \tag{53}$$

Using the definition of velocity in Eqs. (6)–(8), the uncertainty reduces to:

$$\mu_{V_i}^2 = \left(\frac{V_i}{L}B_L\right)^2 + \left(\frac{V_i^2}{L}B_r\right)^2 \tag{54}$$

In Eq. (54) B_L was measured with a Nikon D80 camera with a resolution of 6 μm per pixel. From the picture there the edges of the probe tips were discernable in a distance of about two pixels.

The uncertainty in the average velocity, Eq. (15), adds a random uncertainty resulting in

$$\mu_{\overline{V}}^2 = \left(\frac{\overline{V}}{L}B_L\right)^2 + \left(\frac{\partial V_i}{\partial t}B_r\right)^2 + \left(\frac{T_{v,95}\,s_v}{\sqrt{N}}\right)^2 \tag{55}$$

In Eq. (55) s_v is the standard deviation of the individual bubble velocity measurements and N is the total number of bubbles measured in the trial.

3.6.3. Bubble chord length

The bubble chord length is computed from Eq. (9), and the average chord length from Eq. (16). The propagated error for the chord length is then

$$\mu_{CL}^2 = (\Delta t_i\,\mu_{V_i})^2 + (V_i\,\mu_{\Delta t_i})^2 \tag{56}$$

The time uncertainty $\mu_{\Delta t_i}$ has two main systematic elemental errors,

$$\mu_{\Delta t_i}^2 = B_{tp,i}^2 + B_r^2 \tag{57}$$

$B_{tp,i}$ is the uncertainty in time due to the finite penetration time of the bubble surface, and due to bubble deformation. This error is affected by the digitalization procedure (double threshold in our case) and by the probe geometry (Cartellier and Achard, 1991). Herein we conservatively assume that most of the uncertainty is due to the finite rise time of the signal, computed from

$$B_{tp,i} = \frac{L_{p,eff}}{V_i} \tag{58}$$

where $L_{p,eff}$ is the effective active length of the probe and V_i is the bubble velocity. This piercing time was used by Abuaf et al. (1978) to measure the interface velocity. The effective tip length used for the IIHR probe was 62.5 μm and 125 μm for the RBI probe.

To estimate the uncertainty of the average chord length, a random error is added of the form

$$s_{\overline{\Delta t}} = \frac{T_{v,95}\,s_{\Delta t}}{\sqrt{N}} \tag{59}$$

where $s_{\Delta t}$ is the standard deviation of all the measured time durations. The average chord length uncertainty is then estimated as

$$\mu_{\overline{CL}}^2 = (\overline{\Delta t}\,\mu_{\overline{V}})^2 + (\overline{V}\,\mu_{\overline{\Delta t}})^2 \tag{60}$$

where the uncertainty in the average time in air is

$$\mu_{\overline{\Delta t}}^2 = B_{tp}^2 + B_r^2 + s_{\overline{\Delta t}}^2 \tag{61}$$

where B_{tp} is computed with the average velocity instead of the bubble velocity. Other errors, such as those due to partially pierced bubbles (Carrica et al., 1995), are neglected.

3.6.4. Gas volume fraction

The gas volume fraction is computed as

$$\alpha = \frac{1}{T}\sum_{i=1}^{N}\Delta t_i = \frac{N\overline{\Delta t}}{T} \tag{62}$$

N and T are determined with very little error, so the gas volume fraction uncertainty is

$$\mu_\alpha = \frac{N\mu_{\overline{\Delta t}}}{T} \tag{63}$$

where $\mu_{\overline{\Delta t}}$ is computed using Eq. (61).

3.6.5. Ship speed and probe position

The uncertainty in ship speed was adopted based on estimation by the ship's captain. The ship speed respect to the water varied no more than 0.5 knots above or below the set velocity, resulting in an uncertainty of ±0.25 m/s. The probe location uncertainty in relation to the ship was estimated in ±0.01 m. The probe depth uncertainty in relation to the waterline was caused in addition by pitch, heave and roll of the ship, and wave motions, which were relatively small in the bay and near the coastline where measurements were taken. This error is estimated in ±0.025 m for the calm days and ±0.05 m for the days with more active seas.

4. Results and discussion

Measurements were taken at the bow, masker and transom locations shown in Fig. 2. The positions are non-dimensionalized with the ship length, with the x axis running from bow to stern and the y axis pointing to starboard, with the origin on the forward perpendicular, i.e. the point where the free surface and the bow intersect.

4.1. Measurements at the bow

Measurements at the bow were performed using RBI II and IIHR probes on two different days. Measurements with the RBI probe were performed with a more rippled sea surface, but still essentially calm, while the IIHR probe was used on a calmer day. Due to higher winds and rougher seas, the first day's measurements were performed in Saint Andrews Bay, where algae and other debris were suspended in the water after runoff from the previous day's rain, causing the use of the sturdier RBI II probe. In addition, fresh water from the rain induced less salinity than normal on that day. The following day conditions were much cleaner and calmer and the IIHR probe was used in the gulf. Thus probe RBI II is associated with measurements at the bay with less calm conditions and probe IIHR with measurements at the gulf with calmer conditions.

The probes were located about 3 m downstream of the bow breaking wave. Visual observation indicated unsteady breaking of the bow wave that created air entrainment during the plunging phase of the breaking, resulting in the formation of bubble clouds that traveled downstream. The average period of this unsteady breaking at 5.4 m/s was 2.8 s in head waves, obtained from frequency analysis of the bubble clouds measured on the second day with the IIHR probe, as discussed later in this section. This encounter period corresponds to waves with a wavelength of 35.2 m. In the presence of higher waves, the path of these bubble clouds was more irregular due to less repetitive location of the breaking of the wave. As a consequence, measurements with the RBI II probe not always crossed the path of the bubble clouds, resulting in lower gas volume fractions. In addition, lower salinity in the bay could also result in lower gas volume fractions, as reported in Jeon et al. (2008).

Fig. 11 shows average gas volume fraction, bubble velocity and chord length as a function of depth, lateral position and ship velocity, taken with probes RBI II and IIHR. The gas volume fraction, Fig. 11a, shows significantly smaller values inside the bay, while at the same time showing larger values when running against the waves. Significant periods with the probe out of the water occurred inside the bay for the highest probe positions, as evident
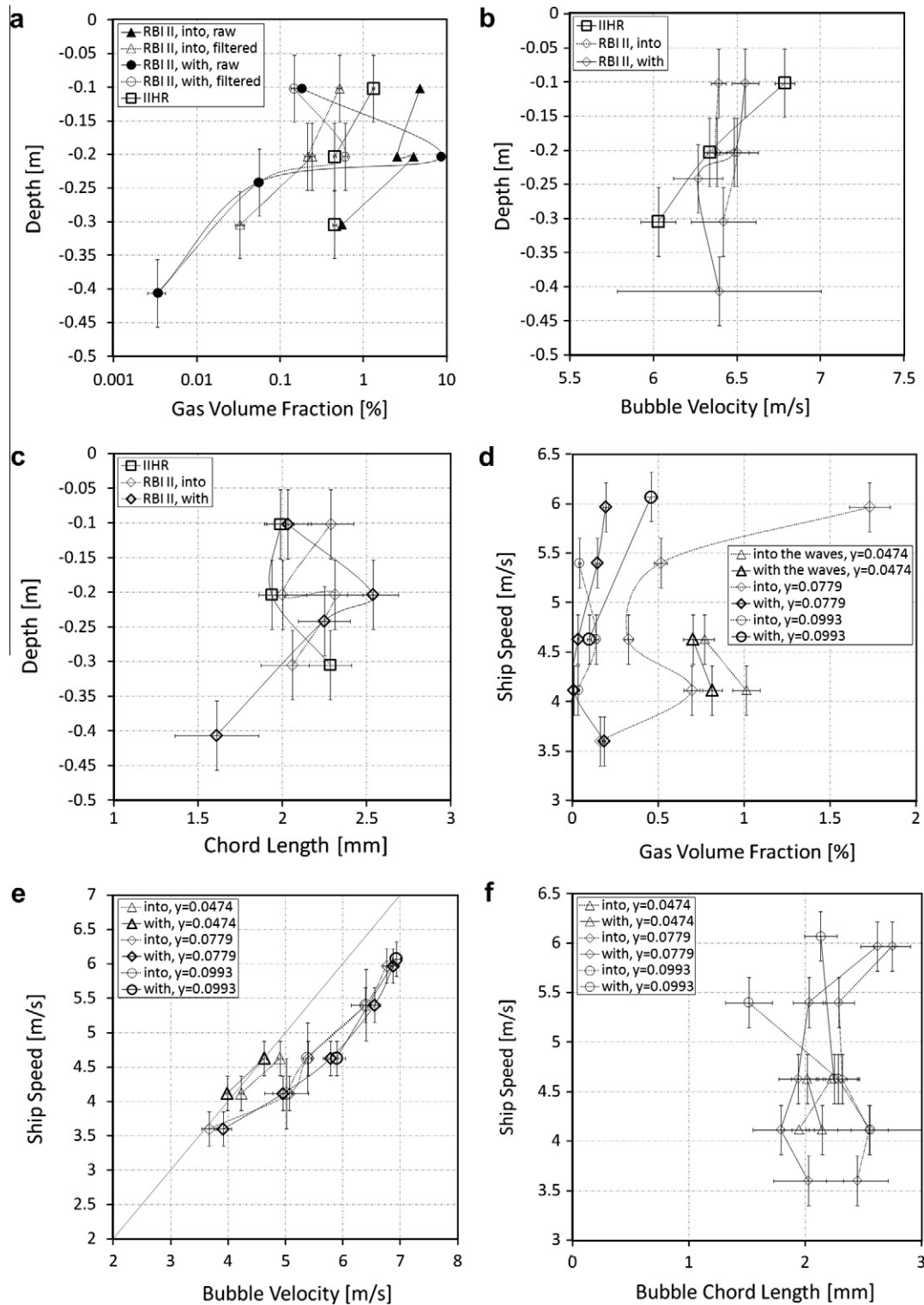
Fig. 11. Measurements at the bow ($x = 0.284$) and at 5.4 m/s unless otherwise specified. Average gas volume fraction (a), bubble velocity (b) and chord length (c) taken with probes RBI II and IIHR at $y = 0.0779$ at different depths. Average gas volume fraction (d), bubble velocity (e) and chord length (f) taken with probe RBI II at 0.1 m below the surface and several ship speeds and distances to the hull.

from the difference between the gas volume fraction computed with the raw indicator functions and the filtered indicator function that removes the time the probe is in air. A clear decay of the gas volume fraction with depth is observed. Gas volume fractions of about 2% are observed in the gulf near the free surface, while values between 0.2% and 0.5% are observed in the bay sailing with and into the waves, respectively.

Bubble velocities, shown in Fig. 11b, are slightly faster than the ship speed of 5.4 m/s, with no significant change when sailing with or into the waves. This higher velocity is most likely due to the fact that the measurement is located at the trough of the bow wave, where water velocities are higher than the ship speed, as shown in Fig. 2 from CFD computations of the flow around the Athena RV sailing at 5.4 m/s (10.5 knots). In addition, acceleration of the

water around the ship will contribute to higher velocities. The IIHR probe clearly shows a trend to lower velocity at deeper locations, where the effects of the water acceleration around the hull and the wave decrease. The average bubble chord length is around 2 mm, with significant scattering around that value, and a slight trend that deeper locations result in smaller average chord lengths, see Fig. 11c.

Effects of ship speed at different locations for measurements in the bay with probe RBI II are shown in Fig. 11d, e and f. Fig. 11d indicates that the gas volume fraction in general increases closer to the hull and with ship speed, as expected. The trend to higher gas volume fractions when sailing into the waves, already observed in Fig. 11a, is repeated here for different ship speeds and distances to the hull. The bubble velocity, shown in Fig. 11e, exhibits higher velocities than the ship at higher distances from the ship, but become smaller closer to the hull, consistent with Fig. 2 but showing higher bubble velocity values than those predicted by CFD and depicted in the figure. The probe positioned at $y = 0.0474$ is about 25 mm away from the hull, where accumulation of bubbles was visually observed, reaching gas volume
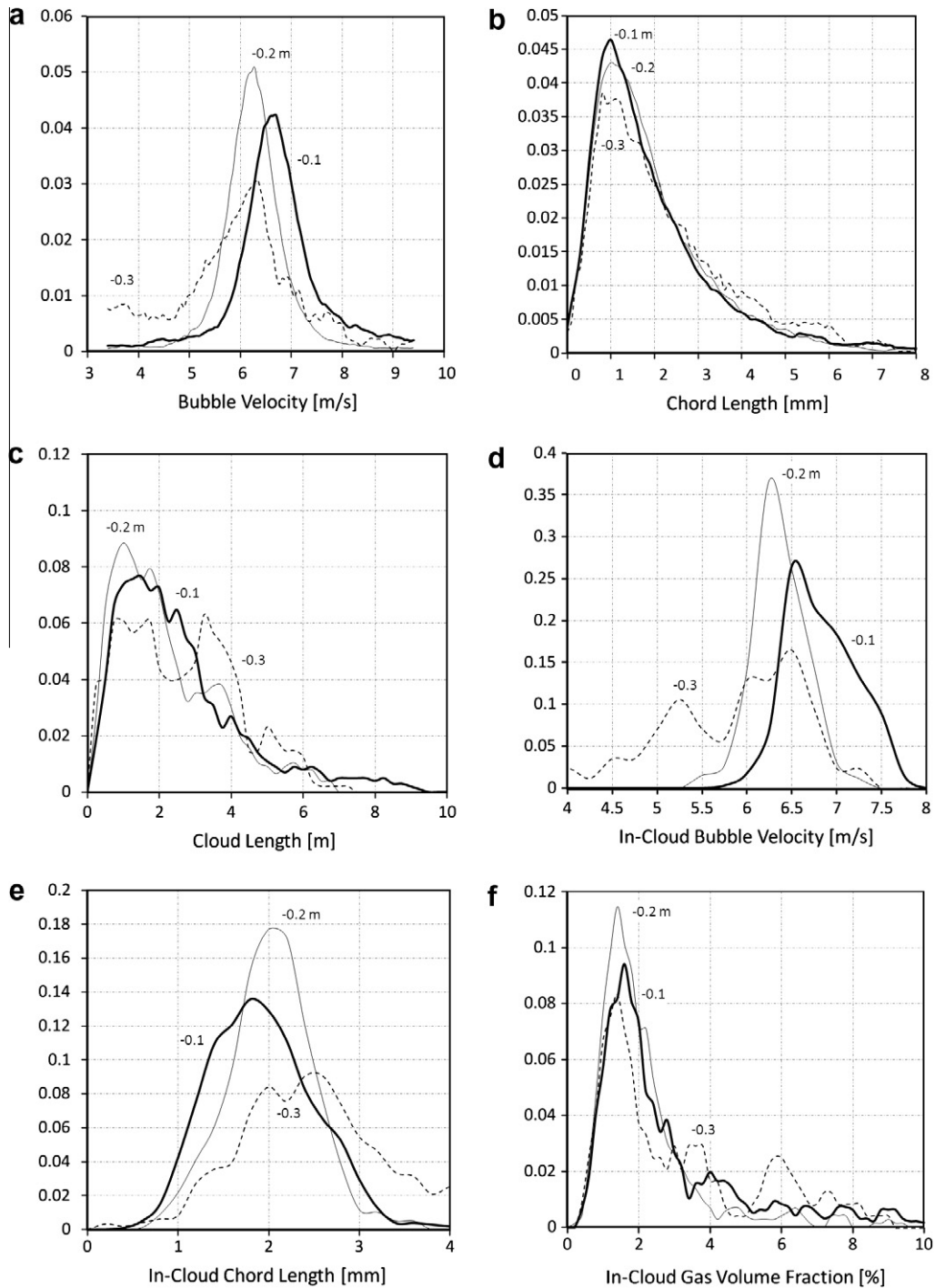
Fig. 12. Bow results with the IIHR probe as a function of depth taken at $x = 0.284$, $y = 0.0779$. (a) Bubble velocity distribution. (b) Chord length distribution. (c) Bubble cloud length distribution. (d) Normalized histogram of the average bubble velocity in each bubble cloud. (e) Normalized histogram of the average chord length within each bubble cloud. (f) Normalized histogram of the average void fraction of each bubble cloud.

fractions close to 1% (see Fig. 11d) and velocities closer to the ship velocity (see Figs. 2 and 11e). Bubble velocities farther out from the ship appear to be faster when sailing with the waves than when sailing into them, with the trend reversed near the hull. These trends are however within the errors of the measurements. At the lowest ship speed the bubble velocity in the ship system decreases significantly, with bubbles moving faster when sailing into the waves, reversing the trend observed for higher ship speeds. This measured trend of bubble velocities closer to the ship velocity when the ship is sailing at slower speeds is likely due to the shortening of the wavelength of the Kelvin wave system as the Froude number decreases, resulting in the probes now measuring closer to a peak of the wave and consequent lower velocities. Though this has not been computed with CFD, an estimation of the wavelength at 3.6 m/s positions the probes right at the second peak of the Kelvin wave system. The average bubble chord length with ship speed, Fig. 11f, shows significant scattering in the data, not revealing a clear trend, suggesting that bubble chord length in the entrainment depth (0.1 m below the surface) is fairly independent of ship speed. Note that the average bubble chord length is heavily biased toward larger bubbles, since the cross section of the bubbles decreases with the radius squared. The average chord length can be viewed as a large-bubble weighted mean.

The RBI II probe finally stopped working after one of the sapphire tips was chipped by debris. The chip can be observed in Fig. 3b.

Fig. 12a and b show distributions of bubble velocity and chord length at three depths, from data taken with the IIHR probe at 5.4 m/s. This probe resulted in much better correlation of the signals between tips than the RBI II probe, and thus better repeatability and consistency of results. The bubble velocity shows a standard deviation respect to the average in the order of ±0.5 m/s at 0.1 m and 0.2 m below the surface, due to turbulent fluctuations and vibrations in the positioning pole. The velocity fluctuations increased significantly at a depth of 0.3 m, likely caused by a very noticeable increase in the vibrations of the pole. Note that the vibrations of the pole should not affect the average value of the velocity. The chord length distributions have similar shapes at all depths, showing a trend toward larger chord lengths at the deepest position, as already reported in Fig. 11c. Note also that although large chord lengths are possible, the maximum probability is for chord lengths of about 1 mm (smaller for the deepest position).

A histogram of the length of the bubble clouds is presented in Fig. 12c. Most probable cloud lengths range from 0.5 to 3 m in length, with some reaching 5 m or more. The statistics are relatively poor since only a few hundred bubble clouds are measured in total, reflecting in the noise observed in the distributions. The distributions of average velocity, average chord length and gas volume fraction within each bubble cloud are shown in Fig. 12d–f. The average bubble velocity in the clouds tends to decrease with depth, while the chord length tends to increase. The same trend was observed for all bubbles in Fig. 12a and b. The average gas volume fraction inside the clouds shows values ranging 0.5–3.5%, peaking around 1.5% and some clouds carrying as much as 6% at 0.3 m depth. Compare these values with the averaged gas volume fraction overall (inside and outside the clouds) shown in Fig. 11a of 1.5% closest to the free surface and 0.7% at the two deeper locations. The much lower averages indicate that most of the bubbles are located inside the bubble clouds.

Fig. 13a shows the frequency spectrum of the gas volume fraction, obtained by integrating the indicator function during a moving window of time T

$$\alpha(\mathbf{r}, t) = \frac{1}{T} \int_t^{t+T} \chi(\mathbf{r}, \tau) d\tau \qquad (64)$$
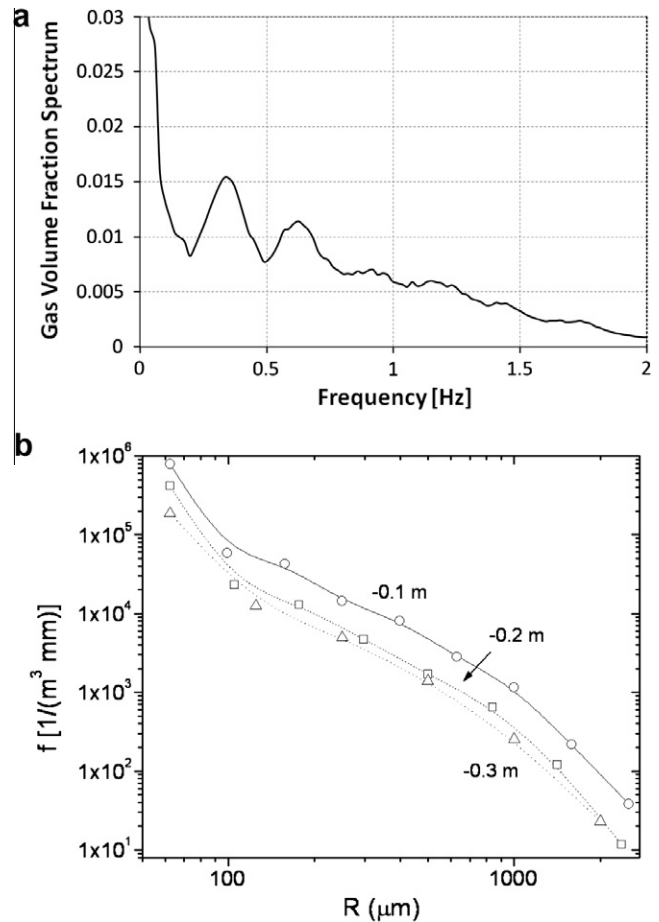

Fig. 13. Bow results with the IIHR probe as a function of depth taken at $x = 0.284$, $y = 0.0779$. (a) Frequency spectrum of the gas volume fraction at depth 0.2 m, showing a peak at a period of about 0.33 Hz. (b) Bubble size distribution of all bubbles measured at each depth.

0.5 s was adopted for the integration time T. This function indicates the probability of finding a bubble during the integration time, and will respond to fluctuations slower than about half the integration period. Fig. 13a clearly indicates a peak response at about 0.36 Hz and harmonics of that frequency, indicating that the dominant period of encounter of the bubble clouds with the probe was about 3 s. These results are consistent with visual observations discussed at the beginning of this section and support an average encounter period of 2.8 s and an average wavelength of 35.2 m.

Bubble size distributions were obtained at the three measured depths, following the procedure described previously. Since the procedure requires large statistics to provide smooth curves, the number of points resolved was limited to nine for the two upper depths and six for the lower position. The results show that the size distributions follow essentially the same curve, scaled with the total gas volume fraction (Fig. 13b). The probe is not small enough to capture the peak in size distribution, with processed sizes down up to 62.5 μm in radius. Using a photographic method in a different location and under different operational conditions, Terril et al. (2005) found a peak for bubbles as small as 15 μm in radius. Unfortunately photographic methods fail for large gas volume fractions (larger than maybe 0.1%) because of shielding between bubbles. To capture bubbles smaller than 15 μm in radius with phase-detection probes, a tip of effective diameter of 15 μm or less would be needed.

4.2. Measurements at the masker

Measurements behind the masker were performed in the gulf with the RBI probe. The masker works by inducing a strong low pressure downstream of a semi-cylindrical ring that runs around the hull, causing strong air entrainment (see Fig. 1) and an unsteady breaking wave running with a very sharp angle respect to the ship axis. Measurements were taken at $x = 0.487$ and at three distances from the hull. Fig. 14a shows the gas volume fraction at different speeds and distances from the hull, as a function of depth. The gas volume fractions are much higher than those measured at the bow, with values reaching 5% or higher. Also of notice is the strongly unsteady location of the free surface, which causes differences between the signals raw and filtered (recall that the filter removes the effects of the probe outside the water) to be different even at depths as deep as 0.4 m, indicating that the masker is sucking air in by forming a deep, unsteady depression in the free surface in the form of a whirlpool. The trends of increasing gas volume fractions with speed and proximity to the free surface are clear in Fig. 14a.

The average bubble velocity, illustrated in Fig. 14b, shows that the bubbles move slightly slower than the ship near the free surface, and that the bubble velocity increases significantly at higher depths and farther out from the hull. The reasons for the bubble velocity increases are unknown and require further investigation,

but a possible cause could be the formation of a large separation region downstream of the masker.

Fig. 14c and d show the average chord length and chord length distributions, respectively. A decrease in chord length with depth is apparent, a trend shown both by the average value as well as in the distributions. The chord lengths are comparable to those measured in the bow, averaging around 2 mm.

Bubble size distributions at $x = 0.487$, $y = 0.0766$ and 5.4 m/s for four depths are shown in Fig. 15. The slope of the curves drops slower than those at the bow, indicating the presence of larger bubbles. Also, as opposed to the bow, the distribution increases more gently for smaller bubbles, showing that there are a relatively smaller amount of very small bubbles. These differences are likely due to the different air entrainment processes in the bow and in the masker, where the presence of the low pressure region in the whirlpool submerges large amounts of big bubbles.

4.3. Measurements at the stern

The stern flow of Athena at low speeds is characterized by a wet transom with a consequent highly ventilated, unsteady roller. The air/water mixture near the free surface flows forward toward the ship and below the high-speed flow coming from the propellers pushes the water downstream at high speed. Since the probes are designed to face the flow tip first, the probe direction was
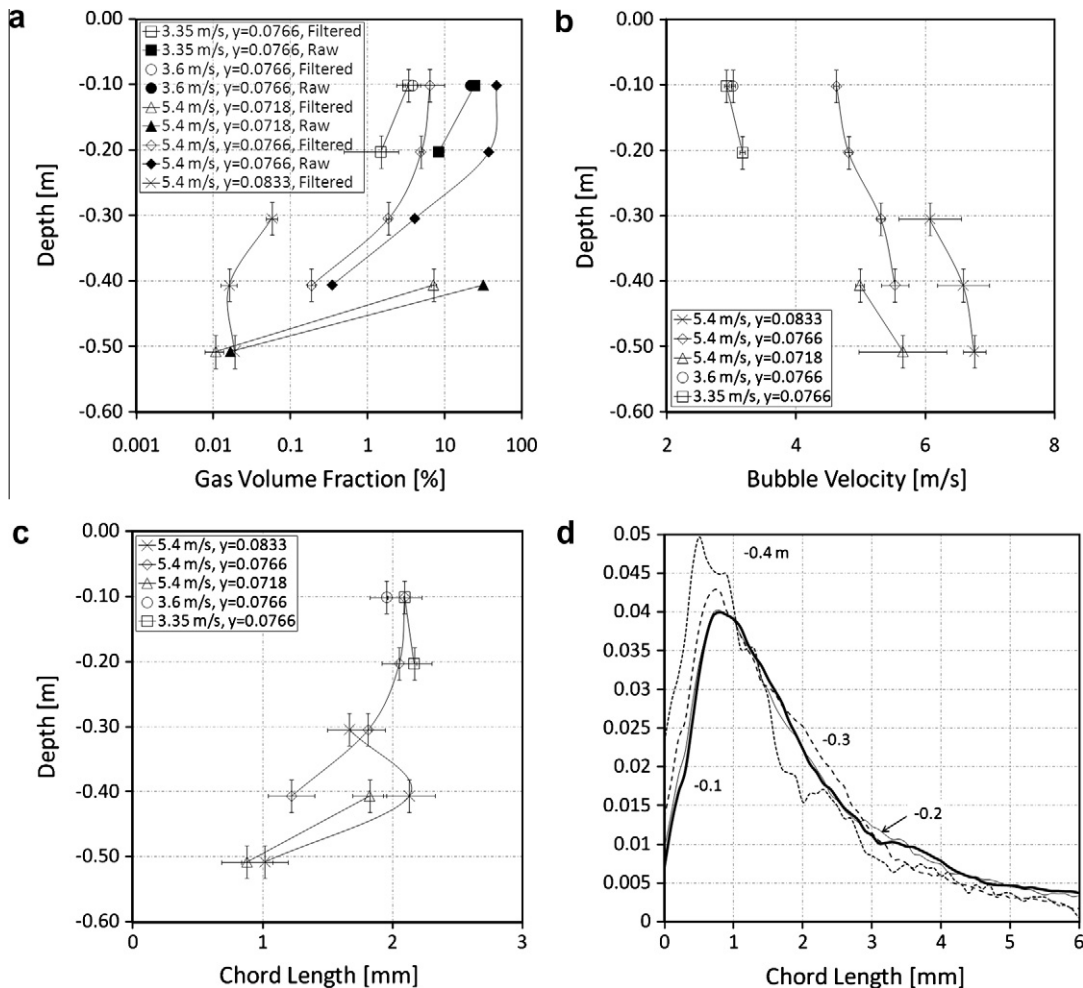

Fig. 14. Results with the RBI probe downstream of the masker at $x = 0.487$. (a) Gas volume fraction for different probe locations and ship speeds. (b) Average bubble velocity for different probe locations and ship speeds. (c) Average bubble chord length measurements for different probe locations and ship speeds. (d) Chord length distribution at $y = 0.0766$ and 5.4 m/s.
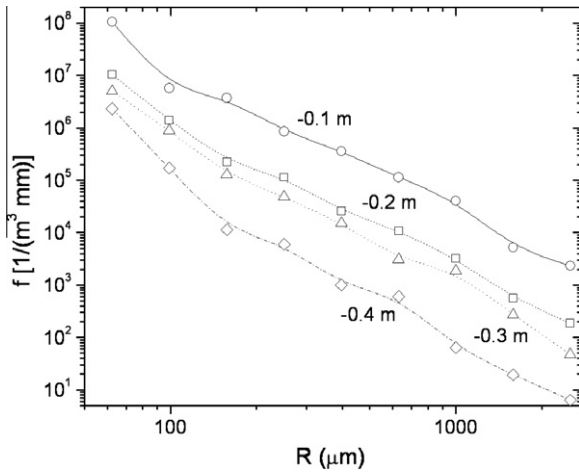
Fig. 15. Bubble size distribution downstream of the masker at $x = 0.487$, $y = 0.0766$ and 5.4 m/s.

inverted for positions 0.6 m below the free surface and lower, with positions −0.6 m and −0.7 m measured with the probe pointing forward and aft.

Measurements were taken with the RBI probe at 4.6 m/s (9 knots) at two axial positions, $x = 1.0173$ and $x = 1.0038$, corre-

sponding to the probe pointing to the stern and to the bow, respectively. The lateral location was $y = −0.021$.

The highly ventilated and unsteady nature of the transom flow makes it difficult to identify the location of the free surface, since the upper air/water mixture is composed by a frothy combination of large bubbles and drops that jumps up and down with an amplitude of over 0.3 m. This is clearly exposed by inspecting Fig. 16a, where at the top location the unfiltered gas volume fraction of 60% decreases to 13% after eliminating the time the probe is above the surface. This difference between unfiltered and filtered gas volume fraction decreases with depth to about zero at $z = −0.5$ m, where the flow becomes bubbly. At approximately $z = −0.55$ m the velocity reverses direction (see Fig. 16b) and measurements are taken with the probe pointing to the bow. Note that aiming the probe to stern or bow changes the axial position of the probe by 0.63 m. Higher gas volume fractions are observed near the hull for the same depth. A change in trend is observed below the roller, where the slope in the log-linear gas volume fraction plot in Fig. 16a increases.

The bubble velocity plot, shown in Fig. 16b, indicates that the bubbles inside the roller move toward the bow at a fairly uniform velocity of about −1.5 m/s, and that after reversing to point downstream the velocity quickly increases to the free stream velocity. Effects of the high-speed wake of the propeller were not observed at this depth, and can be expected about 0.2 m deeper.
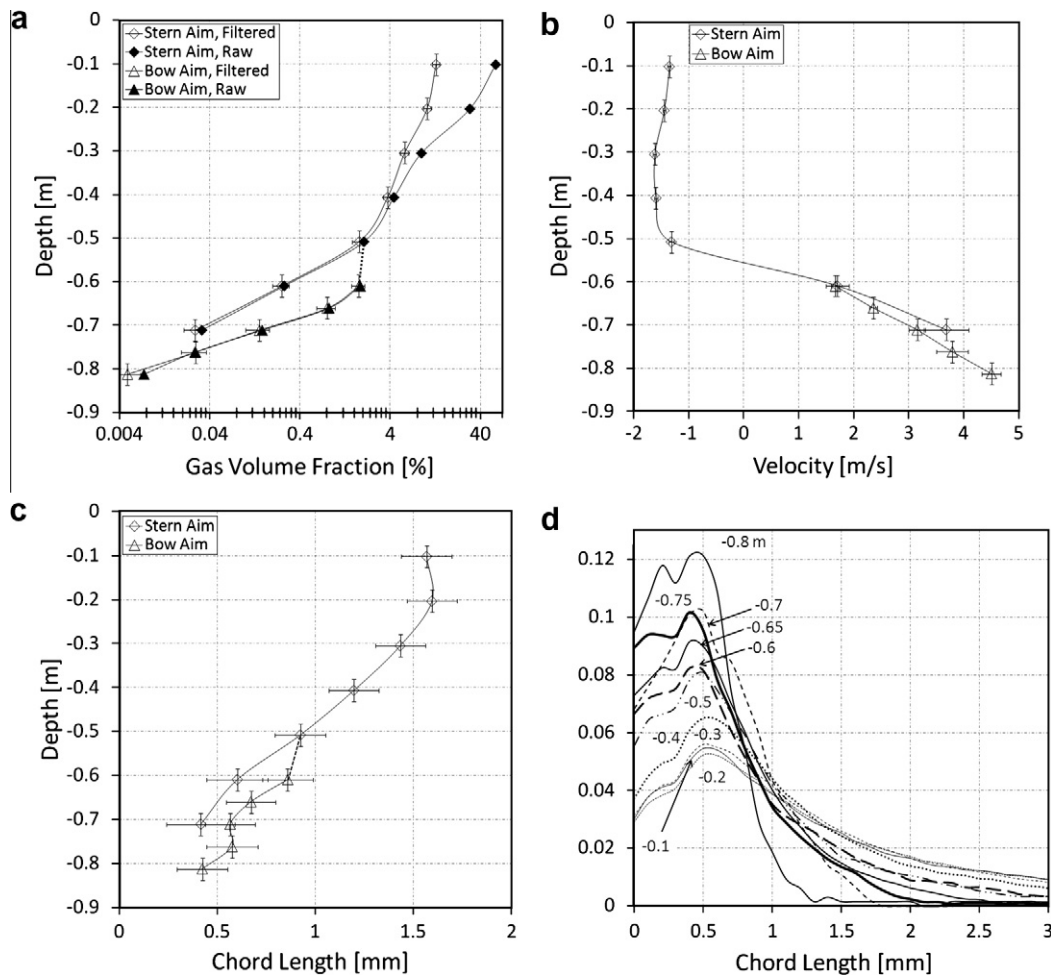

Fig. 16. Stern measurements taken the RBI probe at 4.6 m/s (9 knots). (a) Raw and filtered gas volume fraction. (b) Average bubble velocity. (c) Average bubble chord length. (d) Bubble chord length distribution.

Fig. 16c shows the average bubble chord lengths as a function of depth. Below the point of reversal of velocity direction the chord lengths measured with probe pointing to the bow are more reliable, having been measured with the probe orientation under design conditions, but results for the probe located at $x = 1.0173$ aiming to stern are retained. Notice the considerable decrease in average chord length from over 1.5 mm at the top to below 0.5 mm at the deepest locations.

The trend of smaller bubbles at higher depths reflected in the chord length distributions shown in Fig. 16d, where normalized chord length distributions are shown for depths from $z = -0.1$ m to $z = -0.8$ m, with the probe always oriented against the flow. Chord length distributions are essentially uniform for the shallowest three depths, showing the essentially uniform structure of the two-phase mixture in the roller. Deeper into the flow the distribution moves to smaller chord lengths, tending to show a bimodal distribution for the deeper locations. The resulting bubble size distributions are shown in Fig. 17.

To better visualize the shift from bubbles of large to small size as depth increases, the normalized group gas volume fractions are shown in Fig. 18a. The group gas volume fraction for a group of bubble sizes g is defined as (Carrica et al., 1999)

$$\alpha_g = \int_{r_{g-1/2}}^{r_{g+1/2}} f(r) \frac{4}{3} \pi r^3 dr \qquad (65)$$

where the group g spans from $r_{g-1/2}$ to $r_{g+1/2}$, each of these defined as the radii in Fig. 18a, starting in zero and ending in 5 mm, with distribution functions zero at these two extremes and assumed to change linearly between zero and the first computed radius and the largest computed radius and 5 mm. To produce Fig. 18a the sum of the gas volume fraction of all groups is normalized to 1.

Consistent with Figs. 16d and 17, the gas volume fraction for the first three depths in Fig. 18a is dominated by very large bubbles (about 2 mm in radius), with almost identical distribution of gas volume fraction across the groups. As the measurements are taken
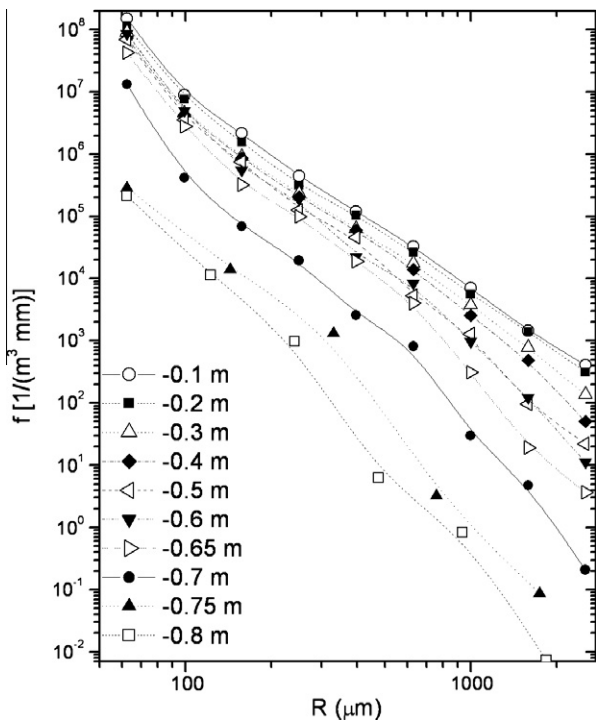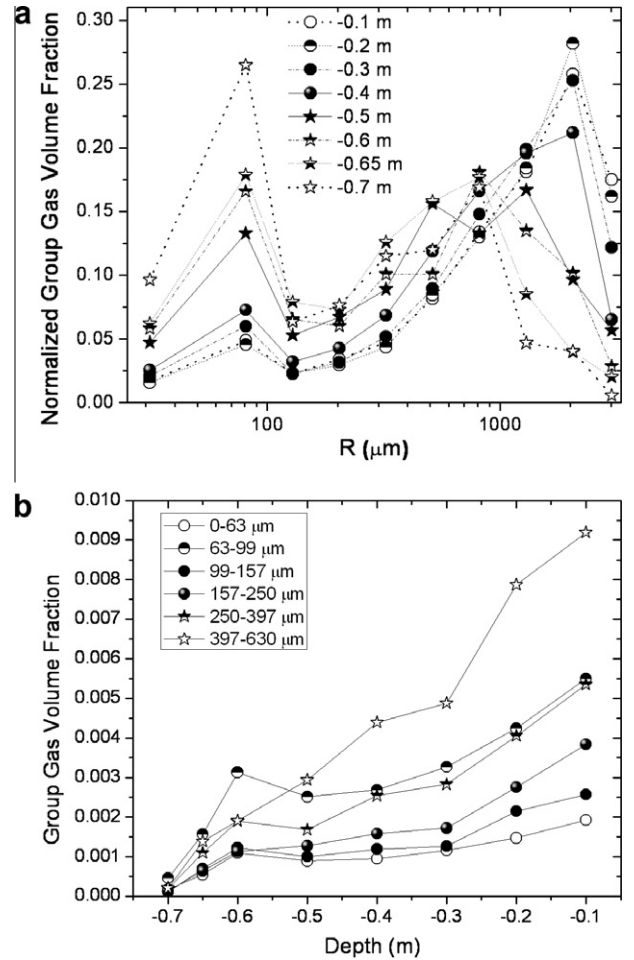
Fig. 18. Normalized group gas volume fraction obtained from the bubble size distributions in Fig. 17 (a), and absolute group gas volume fraction profiles for the six smallest group sizes (b).

Fig. 17. Bubble size distribution at the stern, taken the RBI probe at 4.6 m/s (9 knots).

deeper, the gas volume fraction distribution becomes bimodal, with the peak for the large bubbles shifting to smaller sizes (about 500 μm for the deepest position) and developing a peak at a much smaller size (about 80 μm), which for the deepest position accounts for almost 20% of the gas volume fraction. These results imply that at the deepest location the ratio of bubble number densities between bubbles smaller than 200 μm and bubbles bigger than 200 μm is over 10 times larger than the same ratio at the top three positions.

Several processes could be responsible for the relative increase of small bubbles at deeper locations, and it is of interest to identify the relative importance of each of these processes. The hydrostatic pressure increase with depth will compress the bubbles and reduce their size (and consequently the bubble size distribution and gas volume fraction). For our measurements, however, this effect will result in a change in volume of only 8% at the deepest measurement position, or a change in radius of only 2.6%. Another effect of importance could be turbulent transport of bubbles from the entrainment region in the roller to deeper regions of the flow. Larger bubbles, with higher buoyancy and vertical velocity, are harder to retain deep into the flow, and thus their number density would be lower than smaller bubbles. Though this hypothesis cannot be discarded off-hand, the velocities involved in the stern flow (see Fig. 16b) are much larger than the terminal rise velocities of the bubbles, even the largest ones, that can probably rise at about 0.3 m/s (Clift et al., 1978). Thus it can be expected that bubbles

transported by turbulent diffusion near the transom should not have drastically different bubble size distributions. In addition, the bubble velocity is very large at the deepest positions, suggesting that bubbles carried deep into the flow by turbulent diffusion will be transported out quickly, leaving little time for the large bubbles to rise and leave the deeper locations faster than the smaller ones. At least two other processes could be responsible for the presence of smaller bubbles at depth: the bubbles are entrained somewhere else and transported downstream to the stern, or they were generated by the propeller.

In the first hypothesis, bubbles entrained in the bow breaking wave, masker region and along the contact line between the hull and the free surface can be transported below the hull where they are subject to large shear stress and intense potential breakup, leading to small bubbles finally reaching the stern. These bubbles are present in Fig. 18b, which shows the absolute group gas volume fraction of different sizes as a function of depth. An increase on the gas volume fraction of the smallest bubbles is observed at -0.6 m, where the velocity changes sign at the bottom edge of the transom stern, see Fig. 16b. Though other possibilities could be entertained, this increase in the gas volume fraction of small bubbles can be seen as evidence that bubbles are being transported from upstream below the hull. This increase in gas volume fraction of small bubbles could also be caused by local breakup of bigger bubbles into smaller ones, though the process leading to that breakup is not evident.

Small air bubbles can be generated from small nuclei that grow by absorbing air dissolved in the water in low pressure regions near the propellers. This process has been tested numerically (Hsiao et al., 2006) and proven to result in a significant number of small bubbles, but never tested in the field.

With the objective of evaluating the hypothesis that bubbles are produced by the propellers, a series of runs were performed in which several speeds were tested using the IIHR probe. The measurements were performed in a different day with slightly higher waves than the previously presented stern results, and included runs with and against the waves, and running both and one propeller. During these measurements the downstream tip of the IIHR probe stopped working due to a faulty splice between glass and sapphire caused by excessive vibration. This prevented computations of bubble velocities and size distribution, but gas volume fractions are still valid using the forward tip. The position of the tip was $x = 1.0065$ aiming to the bow, $y = -0.021$.

Fig. 19 shows the results for ship speeds of 5.4 m/s, 4.6 m/s and 3.5 m/s (10.5, 9 and 6.8 knots). The gas volume fraction at higher
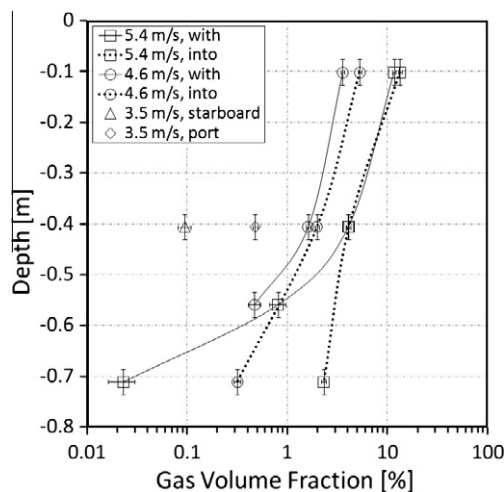
depths shows a significant increase when sailing against the waves, with the values sailing with the waves similar to the calm water results shown in Fig. 16a. This trend could be an indication of increased number of bubbles entrained due to wave breaking and other free surface processes at the bow, masker and contact line, and travelling under the hull to the surface at the stern. Recall that the entrainment at the bow wave showed a considerable increase when sailing against the waves. These results would support the first hypothesis described previously. However, with this limited information no conclusion is possible.

Measurements at one depth were also performed for the ship propelled using either the port propeller (directly upstream of the probe) or starboard propeller. The operational conditions running with a single propeller change in that the rudders have to compensate to maintain the heading. In addition, the maximum speed achievable was 3.5 m/s with the diesel engine running at full power. Fig. 19 shows that the gas volume fraction increases dramatically with the ship sailing only with the propeller from port, the probe side. Since in these conditions (propulsion from starboard or port propellers) the ship speed and heading are identical, it is reasonable to expect that bubbles entrained upstream of the propeller will not be affected by which propeller is used. This seems to indicate that the propellers are effectively generating bubbles that are detected in the stern. These results are, however, inconclusive because the propeller may instead be increasing the turbulence and air entrainment in the transom flow itself, reflecting in the gas volume fraction. An attempt to measure at a higher depth, where bubbles entrained by the transom flow are unlikely to reach, resulted in the positioning pole being bent out of shape and rendering it inoperable.

5. Conclusions

Full scale two-phase flow measurements at the bow breaking wave, masker and stern of the research vessel *Athena II* operating in Saint Andrew Bay and the gulf coast near Panama City, FL, were presented. The data was taken with sapphire optical probes, and processed extensively to obtain gas volume fraction, bubble velocity and bubble size distribution. To obtain the bubble size distribution a novel methodology was introduced, which accounts for the finite size of the probe.

Results at the bow show bubble clouds created by unsteady breaking of the bow wave. Average bubble velocities are slightly larger than the ship speed, caused by acceleration around the hull, and decreasing inside the boundary layer. The bubble clouds have a frequency of about 0.33 Hz, reflecting the encounter frequency of the waves with the ship. In general gas volume fraction was found to increase with ship speed and direction (sailing into the waves) and was also found to decrease with depth. While typical gas volume fractions ranged from 0.1% to 1%, in-cloud gas volume fraction ranged from 1% to 8%. The bubble size distribution exposed a fairly uniform distribution for all depths measured.

Measurements at the masker revealed a highly ventilated and unsteady behavior, with gas volume fractions inside the water well over 1% near the surface. The bubble velocities were found to increase with depth and lateral distance from the hull, both complementing to add to the total distance to the hull. The size distribution shows that near the surface a much larger number of big bubbles were found compared to deeper locations.

The presence of the roller found at the stern at low Froude numbers was detected through direct measurement of the bubble velocity. The frothy flow on the top 0.3 m of the transom flow was measured and characterized, showing very high gas volume fractions that rapidly decay with depth. The average chord length also decays rapidly with depth, to almost 1/4 of the average chord

Fig. 19. Stern measurements taken the IIHR probe at several speeds.

length measured inside the frothy top. The chord length and bubble size distributions show that smaller bubbles (smaller than 500 μm in radius) dominate the deeper regions while larger bubbles (about 2000 μm in radius) make up most of the gas volume fraction on top. Evidence was found showing that the number of small bubbles increases near the bottom edge of the transom stern, suggesting that bubbles slipping below the hull enter the transom flow at the bottom edge. Attempts to measure the presence of bubbles created by the propeller tend to show higher gas volume fraction when the propeller directly upstream of the probe was operated, but these results are inconclusive.

Future work is focused on the development of smaller probes (less than 30 μm including both tips) and designing positioning systems to measure directly downstream of the propellers and inside the boundary layer below the hull. In addition, CFD computations using a polydisperse approach are important to complement the experimental data and provide a basis to better understand the physical processes involved in the interaction of bubbles with a surface ship and to help design future experiments.

Acknowledgements

References

Abuaf, N., Jones, O.C., Zimmer, G.A., 1978. Optical probe for local void fraction and interface velocity measurements. Rev. Sci. Instrum. 49, 1090–1094.

ASME, 2005. Test Uncertainty. ASME PTC 19.1-2005. The American Society of Mechanical Engineers, 102 pp.

Barrau, E., Rivière, N., Poupot, Ch., Cartellier, A., 1999. Single and double optical probes in air–water two-phase flows: real-time signal processing and sensor performance. Int. J. Multiphase Flow 25, 229–256.

Borowski, B., Sutin, A., Roh, H.S., Bunin, B., 2008. Passive acoustic threat detection in estuarine environments. Proc. SPIE 6945, 694513.

Carrica, P.M., Sanz, D., Delgadino, G., Zanette, D., Di Marco, P., 1995. A contribution to uncertainties estimation of local void fraction measurements in gas–liquid flows. In: Int. Symp. Two-Phase Flow Modeling and Experimentation, Rome, Italy.

Carrica, P.M., Bonetto, F., Drew, D., Lahey Jr., R.T., 1998. The interaction of background ocean air bubbles with a surface ship. Int. J. Numer. Methods Fluids 28, 571–600.

Carrica, P.M., Bonetto, F., Drew, D., Lahey Jr., R.T., 1999. A polydisperse model for bubbly two-phase flow around a surface ship. Int. J. Multiphase Flow 25, 257–305.

Cartellier, A., Achard, J.L., 1991. Local phase detection probes in fluid/fluid two-phase flows. Rev. Sci. Instrum. 62, 279–303.

Cartmill, J.W., Su, M.Y., 1993. Bubble size distribution under saltwater and freshwater breaking waves. Dyn. Atmos. Oceans 20, 25–31.

Caruthers, J., Gilbert, K., Stanic, S., 2009. Underwater acoustics and acoustical oceanography: session in honor of ralph goodman and his contributions to the acoustics of bubbles and other works. In: 157th Meeting of the Acoustical Society of America, Portland, OR.

Clark, N.N., Turton, R., 1988. Chord length distributions related to bubble size distributions in multiphase flows. Int. J. Multiphase Flow 14, 413–424.

Clift, R., Grace, J., Weber, M., 1978. Bubbles. Drops and Particles. Dover, Mineola, New York.

Hoschek, S., Carrica, P., Weber, L., 2008. Bubble entrainment and distribution in a model spillway with application to total dissolved gas minimization. J. Hydraul. Eng. 134, 763–771.

Hsiao, C., Jain, A., Chahine, G.L., 2006. Effect of gas diffusion on bubble entrainment and dynamics around a propeller. In: 26th Symposium on Naval Hydrodynamics, Rome, Italy.

Hu, B., Angeli, P., Matar, O.K., Lawrence, C.J., Hewitt, G.F., 2006. Evaluation of drop size distribution from chord length measurements. AIChE J. 52, 931–939.

Hyman, M., 1994. Modeling ship microbubble wakes. CSS/TR-94/39

Ishii, M., 1975. Thermo-Fluid Dynamic Theory of Two-Phase Flow, Eyrolles, Paris.

Jeon, D., Graff, E., Gharib, M., 2008. Measurement of large scale bubbly flows. In: 27th Symposium on Naval Hydrodynamics, Seoul, Korea.

Latorre, R., Miller, A., Philips, R., 2003. Micro-bubble resistance reduction on model SES catamaran. Ocean Eng. 30, 2297–2309.

Liu, W., Clark, N.N., 1995. Relationships between distributions of chords lengths and distributions of bubble sizes including their statistical parameters. Int. J. Multiphase Flow 21, 1073–1089.

Liu, W., Clark, N.N., Karamavruc, A.I., 1998. Relationship between bubble size distributions and chord length distribution in heterogeneously bubbling systems. Chem. Eng. Sci. 53, 1267–1276.

Ma, J., Oberai, A., Drew, D., Lahey Jr., R.T., Hyman, M., 2009. A comprehensive subgrid air entrainment model for Reynolds-averaged simulations of free-surface bubbly flows. In: 62nd Annual Meeting of the APS Division of Fluid Dynamics. Minneapolis, MN.

Moraga, F.J., Carrica, P.M., Drew, D., Lahey Jr., R.T., 2008. A sub-grid air entrainment model for breaking bow waves and naval surface ships. Comput. Fluids 37, 281–298.

Stutz, B., Reboud, J.L., 1997. Experiment on unsteady cavitation. Exp. Fluids 22, 191–198.

Takahashi, T., Kakugawa, A., Makino, M., Kodama, Y., 2003. Experimental study on scale effect of drag reduction by microbubbles using very large flat plate ships. J. Kanai Soc. NA 239, 11–20.

Takeo, U.G.A., 1971. Determination of bubble-size distribution in a BWR. Nucl. Eng. Des. 22, 252–261.

Terril, E.J., Fu, T., 2008. At-sea measurements for ship hydromechanics. In: 27th Symposium on Naval Hydrodynamics. Seoul, Korea.

Terril, E.J., Melville, K., Lada, G., Otero, M., Hazard, J., Harris, T., Pierson, A., Middleton, B., Jenkins, T., 2005. In: 2004 Field Measurements. 2005 ONR Bubbly Flows Program Review. Pasadena, CA.

Vermande, S., Simpson, K., Essemiani, K., Fonade, C., Meinhold, J., 2007. Impact of agitation and aeration on hydraulics and oxygen transfer in an aeration ditch: local and global measurements. Chem. Eng. Sci. 62, 2545–2555.

Yoneda, K., Yasuo, A., Okawa, T., 2002. Flow structure and bubble characteristics of steam-water two-phase flow in a large-diameter pipe. Nucl. Eng. Des. 217, 267–281.